JAMES | Journal of Advances in Modeling Earth Systems®

RESEARCH ARTICLE
10.1029/2024MS004502

Dissipation Scaled Internal Wave Drag in a Global Heterogeneously Coupled Internal/External Mode Total Water Level Model

Coleman P. Blakely[1,2], Damrongsak Wirasaet[1], Albert R. Cerrone[1], William J. Pringle[2], Edward D. Zaron[3], Steven R. Brus[4], Gregory N. Seroka[5], Saeed Moghimi[5], Edward P. Meyers[5], and Joannes J. Westerink[1]

[1]Department of Civil and Environmental Engineering and Earth Sciences, University of Notre Dame, Notre Dame, IN, USA, [2]Environmental Science Division, Argonne National Laboratory, Lemont, IL, USA, [3]College of Earth, Ocean, and Atmospheric Sciences, Oregon State University, Corvallis, OR, USA, [4]Mathematics and Computer Science Division, Argonne National Laboratory, Lemont, IL, USA, [5]Coast Survey and Development Laboratory, National Ocean Service, Office of Coast Survey, National Oceanic and Atmospheric Administration, Silver Spring, MD, USA

Key Points:

- Scaling internal tide dissipation to occur at tidal frequencies, drastically improving global tides in a heterogeneously coupled system
- Baroclinic forcing from an external ocean model improves accuracy of a barotropic model and allows for the capture of long-term sea levels
- Heterogeneous coupling with an ocean global circulation model and a barotropic model efficiently captures density-driven effects

Correspondence to:
C. P. Blakely,
cblakely@anl.gov

Citation:
Blakely, C. P., Wirasaet, D., Cerrone, A. R., Pringle, W. J., Zaron, E. D., Brus, S. R., et al. (2024). Dissipation scaled internal wave drag in a global heterogeneously coupled internal/external mode total water level model. *Journal of Advances in Modeling Earth Systems*, *16*, e2024MS004502. https://doi.org/10.1029/2024MS004502

Received 10 JUN 2024
Accepted 17 NOV 2024

Author Contributions:
Conceptualization: Coleman P. Blakely, Damrongsak Wirasaet, Albert R. Cerrone, Edward D. Zaron, Steven R. Brus, Joannes J. Westerink
Data curation: Coleman P. Blakely
Formal analysis: Coleman P. Blakely, Joannes J. Westerink
Funding acquisition: Gregory N. Seroka, Saeed Moghimi, Joannes J. Westerink
Investigation: Coleman P. Blakely, Damrongsak Wirasaet, Joannes J. Westerink
Methodology: Coleman P. Blakely, Damrongsak Wirasaet, Edward D. Zaron, Joannes J. Westerink

Abstract This study showcases a global, heterogeneously coupled total water level system wherein salinity and temperature outputs from a coarser-resolution (~12 km) ocean general circulation model are used to calculate density-driven terms within a global, higher-resolution (~2.5 km) depth-averaged total water level model. We demonstrate that the inclusion of baroclinic forcing in the barotropic model requires modification of the internal wave drag term to prevent excess degradation of tidal results compared to the barotropic model. By scaling the internal tide dissipation by an easy to calculate dissipation ratio, the resulting heterogeneously coupled model has complex root mean square errors (RMSE) of 2.27 cm in the deep ocean and 12.16 cm in shallow waters for the M_2 tidal constituent. While this represents a 10%–20% deterioration as compared to the barotropic model, the improvements in total water level prediction more than offset this degradation. Global median RMSE compared to observations of total water levels, 30-day sea levels, and non-tidal residuals improve by 1.86 (18.5%), 2.55 (42.5%), and 0.36 (5.3%) cm respectively. The drastic improvement in model performance highlights the importance of including density-driven effects within global hydrodynamic models and will help to improve the results of both hindcasts and forecasts in modeling extreme and nuisance flooding. With only an 11% increase in model run time compared to the fully barotropic total water level model, this approach paves the way for high resolution coastal water level and flood models to be used alongside climate models, improving operational forecasting of total water levels.

Plain Language Summary We showcase a total water level model wherein data from a lower-resolution, 3D ocean model is used to capture changes in density within a higher-resolution 2D total water level model. The inclusion of density-driven effects within the 2D model changes the dynamics of the ocean and necessitates modifications to the internal tide dissipation parameterization in order to accurately capture tides in the coupled system. While purely tidal results are degraded by 10%–20% as compared to the non-coupled model, the resulting system more accurately predicts water levels due to tides, winds, and atmospheric pressure (18%); 30-day mean sea levels (42%); and the meteorologically driven water levels (5%). These improvements help to more accurately predict water levels due to storm events—including hurricanes and tropical cyclones—as well as less deadly but still disruptive flooding seen in coastal communities caused by rising sea levels.

1. Introduction

Total water levels in the ocean and across continental shelves are driven by tides, winds, atmospheric pressure, and thermohaline circulation. How these processes are forced, dissipated, and resolved within a hydrodynamic model is paramount to the resulting model skill. Historically, tides and meteorologically driven water levels have been modeled using higher-resolution, depth-averaged, barotropic models. These models are widely used to predict and capture tides, as well as extreme and nuisance flooding due to their low computational cost and high accuracy (e.g., Bunya et al., 2010; Hope et al., 2013; Westerink et al., 2008, among others). On the other hand, ocean general circulation models (OGCMs) are used to capture low-frequency sea level variations (~10-days to years) that are predominantly density-driven, that is, baroclinic in nature. As such, OGCMs require a large number of vertical layers and sophisticated data-assimilative systems (e.g., 41 layers in Global Ocean Forecasting

Project administration: Gregory N. Seroka, Saeed Moghimi, Edward P. Meyers, Joannes J. Westerink
Resources: Joannes J. Westerink
Software: Coleman P. Blakely, Damrongsak Wirasaet, Albert R. Cerrone
Supervision: Gregory N. Seroka, Saeed Moghimi, Edward P. Meyers, Joannes J. Westerink
Validation: Coleman P. Blakely, Joannes J. Westerink
Visualization: Coleman P. Blakely
Writing – original draft: Coleman P. Blakely, Joannes J. Westerink
Writing – review & editing: Coleman P. Blakely, Damrongsak Wirasaet, Albert R. Cerrone, Edward D. Zaron, Steven R. Brus, Joannes J. Westerink

System (GOFS) 3.1; Metzger et al., 2017). However, for reasons related to computational power and physical scaling, OGCMs typically lack the horizontal resolution required to accurately predict water levels in coastal areas. These disparate scales and physics result in storm surge forecast models failing to capture the very important effect that low-frequency components of sea levels (e.g., seasonal cycle, sea-level rise, variability in major ocean currents) have on extreme and nuisance flooding (Asher et al., 2019). With the changing risks posed by both extreme storm surge and nuisance flooding expected under future climate scenarios, it is vital that hydrodynamic models find methods to incorporate long-term sea levels in order to provide accurate forecasts and hindcasts of coastal water levels (Hsiang et al., 2017; Knutson et al., 2020; Moftakhari et al., 2017; Nicholls et al., 1999).

In recent years, efforts have been made to help bridge the gap between coarse OGCMs with horizontal resolutions generally on the order of tens of kilometers, and higher-resolution coastal total water level models with resolutions up to tens of meters. Slobbe et al. (2013) first demonstrated using OGCM baroclinicity to correct water levels of the 1/8° x 1/12° depth-averaged Dutch continental shelf model to a reference geoid. More recently, W. J. Pringle et al. (2019) incorporated the effects of baroclinicity from the GOFS 3.1 OGCM into a regional depth-averaged total water level model of the Atlantic Ocean with fine (30-m) coastal resolution around Puerto Rico and the U.S. Virgin Islands. In that study, it was found that the inclusion of density-driven effects can improve total water level predictions during hurricane events on coasts with narrow shelves. Taking a different approach, P. Wang et al. (2022) incorporated baroclinicity into a 1/12° global total water level model with a small number of vertical levels (9) by "nudging" temperature and salinity fields from a coarser data-assimilative OGCM. This was shown to improve the modeling of both low-frequency variability and extreme non-tidal water levels. Most recently, Zhang et al. (2023) presented a global model aiming to simulate the entire cross-scale baroclinic-barotropic spectrum in a single unstructured mesh. While successful, significant detailed development remains to reach the respective fidelity of the state-of-the-art OGCM and depth-averaged total water level models.

One obstacle to developing a cross-scale barotropic and baroclinic total water level model is determining an approach to incorporate the dissipation caused by barotropic to baroclinic conversion due to the generation of internal waves. The vast majority of this energy is at the tidal frequencies (i.e., internal tides), which are generated in the deep ocean over regions with steep topographic gradients and at continental shelf breaks (Arbic et al., 2018; Garrett & Munk, 1979). Along with boundary layer dissipation, internal tide dissipation is one of the primary dissipation mechanisms for global tides. The understanding of the importance of internal tide dissipation to the tidal energy balance has greatly expanded in recent years. While early estimates attributed approximately 25%–30% of the 3.5 TW of total tidal dissipation to internal tide dissipation (Egbert & Ray, 2000; Green & Nycander, 2013; Munk, 1997), subsequent studies have indicated that the proportion of tidal energy dissipated in the deep ocean through barotropic to baroclinic conversion could be 40% or higher (Blakely et al., 2022).

As was recently summarized by Arbic (2022), multiple schools of thought exist as to how best to capture this phenomenon. Several studies have argued that their fully three-dimensional models capture internal tides and the resulting dissipation caused by them (P. Wang et al., 2022; Zhang et al., 2023), making parameterizations of internal tide dissipation unnecessary. Other ocean modelers have argued that the resolution of these OGCMs is still not adequate to fully capture internal tides, leading them to apply parameterized wave drag to the bottom layer of the tidal velocity component (Arbic & Garrett, 2010) in order to better capture the energetics of the ocean.

Further complicating the inclusion of internal wave drag in global ocean models is the fact that dissipation occurs through a separate but interdependent mechanism between internal tides and geostrophic lee waves (Shakespeare, 2020). The energy into lee waves has been estimated at 0.2 TW, 20% of global wind power input into the ocean, with the largest component of lee wave energy in the Southern Ocean (Nikurashin & Ferrari, 2011). This is important, but significantly less than the ∼1–1.5 TW estimated for internal tide energy. For depth-averaged, purely barotropic global hydrodynamic models, this does not pose a problem for accurately parameterizing the energy lost due to barotropic to baroclinic conversion. In such models, the deep-ocean depth-averaged velocity is driven almost entirely by the equilibrium tide and, as such, the tidal velocity is well approximated by the total velocity, especially in areas where internal tides dissipation predominantly occurs. This fact means that the internal wave drag can simply be applied to the total velocity in the model without any frequency dependencies. When density-driven, baroclinic effects are incorporated into ocean models, however, this straightforward approach will not accurately capture the dissipation caused by barotropic to baroclinic conversion. This is due to the deep-ocean velocities in such models including the influence of

density-driven thermohaline effects. These higher velocities, in turn, result in total kinetic energy in the ocean model being ∼one to two orders of magnitude higher than a corresponding barotropic model. As a result, when internal tide parameterizations are applied to the full baroclinic velocity, they dissipate not only at the tidal frequencies at which internal tides are generated, but also at the longer frequencies (on the order of weeks to months) at which baroclinic effects occur (Arbic & Garrett, 2010). Due to the highly sensitive response of modeled tides to changes in internal tide dissipation (Blakely et al., 2022), this change in dissipation greatly alters and degrades the quality of the modeled tides.

In this work, we detail our approach to incorporating baroclinic effects and correctly parameterizing internal tide dissipation within a global, depth-averaged, total water level model. This involves expanding upon the work performed in W. J. Pringle et al. (2019), wherein temperature and salinity fields from a relatively coarse OGCM were used to calculate the baroclinic terms, namely the depth-averaged baroclinic pressure gradients and bouyancy frequencies used within the internal tide dissipation parameterization, used within a higher-resolution, regional depth-averaged total water level model in a heterogeneously coupled system. By extending the model domain from a regional case to a global domain, improving the downscaling used in calculating density-driven terms, and most importantly by scaling the internal tide dissipation tensor by a single parameter—the ratio of an estimated tidal dissipation and the total dissipation—we are able to preserve the fidelity of our tidal results while simultaneously incorporating the processes which drive long-term sea levels within the global ocean without incurring the high computational cost and difficult development and deployment that would be required for a correspondingly higher-resolution, fully three-dimensional hydrodynamic model. This heterogeneously coupled system, which was developed in support of the National Oceanic and Atmospheric Administration's Global Surge and Tide Operational Forecast System 2-D (STOFS-2D-Global, available from https://registry.opendata.aws/noaa-gestofs/), allows for highly efficient modeling of total water levels for both hindcasting and forecasting purposes.

The remainder of this study is structured as follows. First, the numerical model and implementation of the one-way, heterogeneous coupling are described in Section 2. This includes a description of the governing equations that are solved; the approach used to calculate the baroclinic terms used within the model from salinity and temperature fields from an OGCM; and the modifications made to the parameterization of internal tide dissipation necessary to accurately capture tides within the coupled model. Next, Section 3 details the development of the computational mesh used for this study; the simulations performed in both barotropic and baroclinically coupled modes; and the measures used to evaluate performance. Section 4 presents the results of three-year hindcasts performed on both our barotropic global model developed in Blakely et al. (2022) and our baroclinically-coupled global model. Finally, Section 5 discusses our results as well future paths of inquiry that are revealed in this study.

2. Numerical Model and Modifications

2.1. Governing Equations

For this global study, a modified version of the ADvanced CIRCulation (ADCIRC) model (Luettich & Westerink, 1992) version 55 (W. J. Pringle et al., 2021) was used. Although ADCIRC does have a fully three-dimensional mode, this study instead uses a heterogeneously coupled system wherein temperature and salinity fields from GOFS3 (Metzger et al., 2017) are used to calculate the density-driven terms in depth-averaged form and used within the 2D ADCIRC model. This methodology was previously used in a regional study and shown to improve non-tidal water levels in a regional case study (W. J. Pringle et al., 2019). However, the shift to a global domain necessitated further modification in order to accurately model the global ocean, which we detail here. Hereafter, barotropic ADCIRC will be referred to as "ADCIRC2D" and the coupled model will be referred to as "ADCIRC2D^{+}." ADCIRC is a widely used hydrodynamic model which solves the Generalized Wave Continuity Equation (GWCE) (Lynch & Gray, 1979), a reformulation of the Shallow Water Equations (SWEs) which can be written as:

$$\frac{\partial \eta}{\partial t} + \nabla \cdot (\boldsymbol{U}H) = 0 \tag{1}$$

$$\frac{\partial \boldsymbol{U}}{\partial t} + \boldsymbol{U}\cdot\nabla\boldsymbol{U} + f\mathbf{k}\times\boldsymbol{U} = -\nabla\left[\frac{p_s}{\rho_0} + g(\eta - \eta_{EQ} - \eta_{SAL})\right] + \frac{\boldsymbol{M}}{H} - \frac{\mathrm{BPG}}{H} + \frac{\boldsymbol{\tau}_s - \boldsymbol{\tau}_b}{\rho_0 H} - \gamma_D\mathbb{C} \tag{2}$$

where η is the free surface elevation (water elevation or sea level); $H(= h + \eta)$ is the total water depth, where h is the still-water depth; $\boldsymbol{U}$ is the depth-averaged velocity vector; $f(= 2\Omega \sin\phi)$ is the Coriolis parameter, where Ω is the angular speed of the earth and ϕ is latitude; $\mathbf{k}$ is the vertical unit vector; p_s is atmospheric pressure at the free surface; ρ_0 is a chosen reference density after making the Boussinesq approximation; g is the acceleration due to gravity; η_{EQ} is the equilibrium tidal potential (Luettich & Westerink, 1992); η_{SAL} is the self-attraction and loading term interpolated from FES2014 (Lyard et al., 2006); $\boldsymbol{M}$ is the lateral mixing term; BPG is the depth-integrated baroclinic pressure gradient as described in Section 2.2; $\boldsymbol{\tau}_s$ is free surface stress due to winds computed using Garratt's drag law (Garratt, 1977); $\boldsymbol{\tau}_b\left(=c_f\rho_0|\boldsymbol{U}|\boldsymbol{U} = \frac{gn^2}{H^{1/3}}\rho_0|\boldsymbol{U}|\boldsymbol{U}\right)$ is bottom stress calculated using and the quadratic drag law, with drag coefficient c_f calculated from Manning's n coefficient and water column depth; $\mathbb{C}$ is the internal tide tensor and γ_D is an adjustment to account for the energy of the baroclinic mode as described in Section 2.3. Note that the momentum dispersion due to varying velocities at different depths as described in W. J. Pringle et al. (2019) was found through sensitivity tests (not shown) to have little to no effect on the results of ADCIRC2D$^+$.

2.2. Depth-Integrated Baroclinic Pressure Gradient

The depth-integrated baroclinic pressure gradient—separated into "rigid lid" (*rl*) and "surface" (*sf*) components—is calculated as:

$$\begin{aligned}\mathrm{BPG} &= \mathrm{BPG}_{rl} + \mathrm{BPG}_{sf}\\ &= \int_{-h}^{\eta} g\nabla\left[\int_z^{\eta}\frac{\rho-\rho_0}{\rho_0}dz'\right]dz\\ &= \frac{g}{\rho_0}\left[\int_{-h}^{0}\nabla\left[\int_z^{\eta}(\rho-\rho_0)\,dz'\right]dz + \int_0^{\eta}\nabla\left[\int_z^{\eta}(\rho-\rho_0)\,dz'\right]dz\right]\\ &\approx \frac{g}{\rho_0}\left[\int_{-h}^{0}\nabla\left[\int_z^{0}(\rho-\rho_0)\,dz'\right]dz + \eta\nabla[\eta(\rho_s-\rho_0)]\right]\end{aligned} \tag{3}$$

where ρ is the density at depth z; and ρ_s is the density at the surface. It is assumed on the interval $z = [0,\eta]$ that $\rho = \rho_s$. We neglect the contribution of baroclinic pressure on $[0,\eta)$ to BPG_{rl} and use numerical integration to estimate BPG_{sf}.

Although physically speaking, BPG is an internal forcing, in ADCIRC2D$^+$, it is calculated from an external OGCM (GOFS3.1) and applied as an extra forcing term in the SWEs. This approach is similar to an internal/external mode coupling except it is heterogeneous and is more efficient at higher spatial resolutions. BPG is calculated using reconstructed densities from GOFS3.1 salinity and temperature fields.

This reconstruction is performed using the GSW Oceanographic Toolbox (McDougall & Barker, 2011), which allows the conversion of GOFS3.1 practical salinity and temperature to the conservative values absolute salinity (S_A) and conservative temperature (Θ). Following this conversion, S_A and Θ are bilinearly interpolated from the rectilinear GOFS3.1 grid to each ADCIRC vertex at each output z-level which is shallower than the depth at the ADCIRC vertex. In cases where the ADCIRC depth is greater than the deepest GOFS3.1 output level (5,000 m), all output levels of GOFS3.1 are used and BPG is integrated from the surface down to the maximum output level. These S_A and Θ profiles are converted to density profiles using the GSW Toolbox. This approach alleviates the bathymetric mismatch between the coarser OGCM and the higher-resolution depth-averaged total water level model and prevents large baroclinic forcing at the coastlines of the higher-resolution model.

Once density profiles at each ADCIRC vertex are calculated, the baroclinic pressure gradients at each GOFS 3.1 24-hourly timestep are calculated in a finite-element sense consistent with the methodology used in full three-dimensional ADCIRC (see Luettich and Westerink (1992) for more details).

2.3. Internal Tide Dissipation

The internal wave drag tensor/internal tide dissipation tensor $\mathbb{C}$ in the momentum equation (Equation 2) parameterizes the energy loss from the barotropic mode caused by barotropic to baroclinic conversion. This dissipation mechanism is vital to capture in order to accurately predict global tides within barotropic models (Arbic, 2022). In ADCIRC2D$^+$, a "local," directional parameterization which takes into account only local topographic gradients and assumes that internal tides are generated only across slopes is used (Lyard et al., 2006; W. J. Pringle, Wirasaet, Suhardjo, et al., 2018; W. J. Pringle, Wirasaet, & Westerink, 2018):

$$\mathbb{C} = \begin{cases} \gamma_D C_{it} \dfrac{\sqrt{\left(N_b^2 - \omega^2\right)\left(\overline{N}^2 - \omega^2\right)}}{\omega} \begin{bmatrix} h_x^2 & h_x h_y \\ h_x h_y & h_y^2 \end{bmatrix} \cdot \boldsymbol{U} & : \ \omega > f \ \& \ h > 150 \text{ m} \\ 0 & : \ \text{otherwise} \end{cases} \tag{4}$$

where, γ_D is an adjustment to the internal tide tensor discussed below; C_{it} is a scaling factor on the order of $\sim 1.0 - 5.0$; N_b is the bouyancy frequency at the base of the water column; $\overline{N}$ is the depth-averaged bouyancy frequency; ω is the dominant tidal frequency (M_2 for this study); h_x and h_y are the bathymetric slopes; and $\boldsymbol{U}$ is the depth-averaged velocity. Both depth-averaged and bottom bouyancy frequencies are calculated from the OGCM using the same profiles as are used to calculate BPG. Internal wave drag is limited to waters that have bathymetric depths greater than 150 m due to boundary layer dissipation becoming the predominant dissipation mechanism in shallow waters (W. J. Pringle, Wirasaet, Suhardjo, et al., 2018).

While internal waves (and thus internal wave drag) can occur due to mesoscale eddying, in the deep ocean, internal waves are generated predominantly at tidal—specifically diurnal and semidiurnal—frequencies (Arbic, 2022; Egbert & Ray, 2000). Thus, internal wave drag parameterizations are designed to act only on the dominant (generally taken to be the M_2) tidal frequency. In barotropic models, it is assumed that the depth-averaged velocity is close to the so-called "tidal" velocity due to the omission of density-driven terms in the governing equations and the generally small barotropic wind-driven component in the deep ocean outside the high latitudes (Carrère & Lyard, 2003) (where internal tide drag becomes zero as $\omega \leq f$). In models which include baroclinic terms, however, this assumption no longer holds true and modifications to the internal wave drag parameterization are necessary to handle the subtidal energy introduced by BPG forcing and correctly capture the energy lost from the barotropic to baroclinic mode. In order to ensure that internal wave drag in the deep ocean is applied at the appropriate frequencies, ADCIRC2D$^+$ scales the internal tide tensor by the ratio γ_D of an estimated "tidal" dissipation due to wave drag to the "total" dissipation due to wave drag, which is calculated as:

$$\begin{aligned} \gamma_D &= \frac{\text{Diss}_{tidal}}{\text{Diss}_{total}} \\ &= \frac{\boldsymbol{U}_{tidal} \cdot \mathbb{C} \cdot \boldsymbol{U}_{tidal}}{\boldsymbol{U} \cdot \mathbb{C} \cdot \boldsymbol{U}} \\ &= \frac{h_x^2 u_{tidal}^2 + 2 h_x h_y u_{tidal} v_{tidal} + h_y^2 v_{tidal}^2}{h_x^2 u^2 + 2 h_x h_y u v + h_y^2 v^2} \end{aligned} \tag{5}$$

where,

Diss_{tidal} = estimated dissipation due to internal wave drag at tidal frequencies.

Diss_{total} = dissipation due to internal wave drag with full depth-averaged velocity

$\boldsymbol{U}_{tidal}$ = estimated tidal velocity vector composed of zonal (u_{tidal}) and meridional (v_{tidal}) components.

To estimate the tidal velocity it is assumed that the depth-averaged velocity is composed of a mean flow $(\overline{\boldsymbol{U}})$ and a tidal flow $(\boldsymbol{U}_{tidal})$:

$$\begin{aligned} \boldsymbol{U} &= \overline{\boldsymbol{U}} + \boldsymbol{U}_{tidal} \\ \boldsymbol{U}_{tidal} &= \boldsymbol{U} - \overline{\boldsymbol{U}} \end{aligned} \tag{6}$$

The mean flow is estimated via a 25-hr lagged average filter (Arbic et al., 2010) and the tidal velocity is estimated by subtracting the mean flow from the total velocity. In order to handle the numerical issues posed when Diss_{total} becomes very small, γ_D is set to 0 when $\text{Diss}_{total} < 1 \times 10^{-10}$ Wm^{-2}. This limit is numerically consistent with the formulation of the internal wave drag parameterization since $\text{Diss}_{total} \approx 0$ means that the depth-averaged velocity is close to 0, resulting in no internal wave drag. Additionally, a cap is set on γ_D of 1×10^2. This value was determined by varying the cap between 1 and 1×10^3, with the maximum value of 1×10^2 selected because it best preserved the behavior seen when varying global C_{it} values in the ADCIRC2D model.

This approach is highly numerically desirable because it ensures that the internal wave drag tensor remains positive semidefinite. This means that the internal wave drag term within the momentum equation is truly dissipative and will not cause the stability issues that would be caused by altering the individual tensor elements or introduce "antidissipation" which could create spurious modes within the solution. In essence, the γ_D parameter forces the dissipation within ADCIRC2D$^+$ due to the internal wave drag parameterization to approach the estimated tidal dissipation, resulting in a more correct representation of barotropic to baroclinic conversion and thus a better representation of global tides.

3. Computational Domain and Simulations Performed

3.1. Computational Mesh and Model Setup

The unstructured mesh used in this study is a slight modification of the mesh used in Blakely et al. (2022). This mesh was generated using OceanMesh2D V3.3 (Roberts et al., 2019) and contains 3.7 million nodes and 7.1 million elements. The resolution of the mesh ranges from 25 km in the deep ocean to 2 km in coastal zones and near steep topographic gradients such as continental shelves and mid-ocean ridges.

For ADCIRC2D simulations, "optimal" frictional coefficients (Manning's n and C_{it}) from Blakely et al. (2022) are used. These values were obtained by first finding spatially constant, global values for both Manning's n and C_{it} which minimized the tidal errors of the model. Once these optimal values were found, the model domain was divided into various regions for both bottom friction and internal tide dissipation. An error minimization technique which used the response to perturbations of friction within these regions was used to find spatially varying friction coefficients which minimize the error in the M_2 tide.

In the case of ADCIRC2D$^+$, Manning's n from the ADCIRC2D simulation was used as they are consistent with bottom roughness and tidal energetics; however, due to the inclusion of baroclinic forcing, C_{it} values needed to be changed due to the changes in dynamics. First, a globally optimum C_{it} value was found. Basin-scale regions were defined and optimal values were estimated using frictional perturbation and the same error minimization technique described in Blakely et al. (2022).

3.2. Simulations Performed

For this study, ADCIRC2D and ADCIRC2D$^+$ simulations are performed covering the time period 1 January 2017–31 December 2019. The time period of 3 October 2016–31 December 2016 is used for model "spin-up" to allow 90-days for the total kinetic energy to reach equilibrium and for the baroclinic engine to drive the global thermohaline circulation. This spin-up period is longer than we typically use in a barotropic simulation due to the presence of low frequency baroclinic currents in ADCIRC2D$^+$. The equilibrium tide (η_{EQ}) is forced using the eight major tidal constituents (M_2, Q_1, O_1, P_1, K_1, N_2, S_2, and K_2) as well as four long-term constituents—fortnightly (Mf), monthly (Mm), solar semiannual (Ssa), and solar annual (Sa). Nodal factors and equilibrium arguments for each constituent is calculated at the midpoint of each simulation year and is used for the entire year.

Atmospheric forcing (p_s and $\boldsymbol{\tau}_s$) is computed from NCEP Climate Forecast System Version 2 (CFSv2) reanalyzes (Saha et al., 2014). Additionally, the effects of ice coverage are included by interpolating CFSv2 ice coverage

fields and increasing the drag coefficient in areas with sea ice (Joyce et al., 2019). For ADCIRC2D, decadally averaged climatology from the World Ocean Database (Boyer et al., 2013) was used to parameterize internal tide dissipation while, as mentioned in Section2.3, bouyancy frequencies calculated from GOFS3.1 were used in ADCIRC2D$^+$

Both ADCIRC2D and ADCIRC2D$^+$ use a time step of 30 s, Smagorinsky lateral mixing coefficient of 0.2, and temporal weighting within the GWCE of 0.05. The model simulations are performed in a rotated spherical coordinate system wherein the poles are located overland, eliminating the singularity that would normally occur (W. J. Pringle et al., 2021). Harmonic analyses reported in Section 4.1.1 used the same forcing and spin-up period, however the harmonic analyses were output after only 45 days because the primary interest was in the M_2 tidal amplitude.

3.3. Measures of Model Skill

In order to assess the performance of the two ADCIRC models, we evaluate the accuracy of model tides; total water levels (η_{TWL}), defined as the water surface elevation as a result of the combined influence of tides, winds, atmospheric pressure, and density-driven forcing; long-term sea levels $(\overline{\eta}_{30})$ calculated as a moving 30-day mean of total water levels; and non-tidal residuals (η_{NTR}), defined as the difference between total water level and a resynthesized harmonic decomposition of the total water level calculated using UTide (Codiga, 2011). Modeled tides are calculated using harmonic decomposition and are assessed both globally—compared to TPXO9-atlas (hereafter TPXO9), a highly accurate data assimilative global tidal model (Egbert & Erofeeva, 2002)—and at a collection of global tide gauge data sets (W. J. Pringle, 2017) which contain harmonic analyses of observed water levels up to 19 years in length. Total water level, long-term sea levels, and non-tidal residuals are compared to observed sea level records compiled in the Global Extreme Sea Level Analysis version 3 (GESLAv3) (Haigh et al., 2022). For both the global tide gauge data set as well as GESLA, stations which fall outside of the mesh triangulation, that is, any station which is not contained within a mesh element, is removed. Additionally, only GESLA records which have observations during the hindcast time period are retained. This leaves a total of 1,809 (out of 2,817) tide gauge stations from W. J. Pringle (2017) and 568 (out of 5,119) GESLA total water level records. While the minimum resolution of the ADCIRC mesh (2 km) is significantly higher than standard OGCMs, it is still too coarse to resolve complex coastal inlet systems such as areas behind barrier islands. Rather than remove stations which fall within the mesh triangulation but which we judge to be resolution limited, we instead leave these stations in and report both mean and median statistics to present a clear picture of model performance.

Additional comparisons are made between ADCIRC2D$^+$ and GOFS3.1 with regards to performance in modeling both non-tidal residuals and 30-day mean water levels. Due to the lack of tidal forcing in GOFS3.1, it is not possible to compare total water levels; however, one can think of the sea-surface heights recorded in GOFS3.1 output as equivalent to non-tidal residuals and take the 30-day moving average to calculate the mean sea level. Because GOFS3.1 is coarser than the ADCIRC mesh, further GESLA records are removed due to falling outside of the GOFS3.1 domain. Most of the stations are, as would be expected, in complex coastal zones which are not resolved in GOFS3.1. After removal, a total 281 GESLA records are used to compare GOFS3.1 and ADCIRC2D$^+$.

Global tidal errors are reported as the mean discrepancy (D) (X. Wang et al., 2012) as compared to TPXO9. TPXO9 is widely used when evaluating tidal results due to its high accuracy at open water tide gauges. D_{tpxo9} was calculated globally; for deep waters (≥1000 m) equatorward of 66° latitude; and for shallow waters (<1000 m) equatorward of 66° latitude. These error metrics are calculated as:

$$D = \sqrt{0.5\sum_k \left[\left(A_o^k\right)^2 + \left(A_m^k\right)^2 - 2A_o^k A_m^k cos\left(\theta_o^k - \theta_m^k\right)\right]} \tag{7}$$

$$\overline{D}_{tpxo9} = \frac{\sum_i A_i D_i}{\sum_i A_i} \tag{8}$$

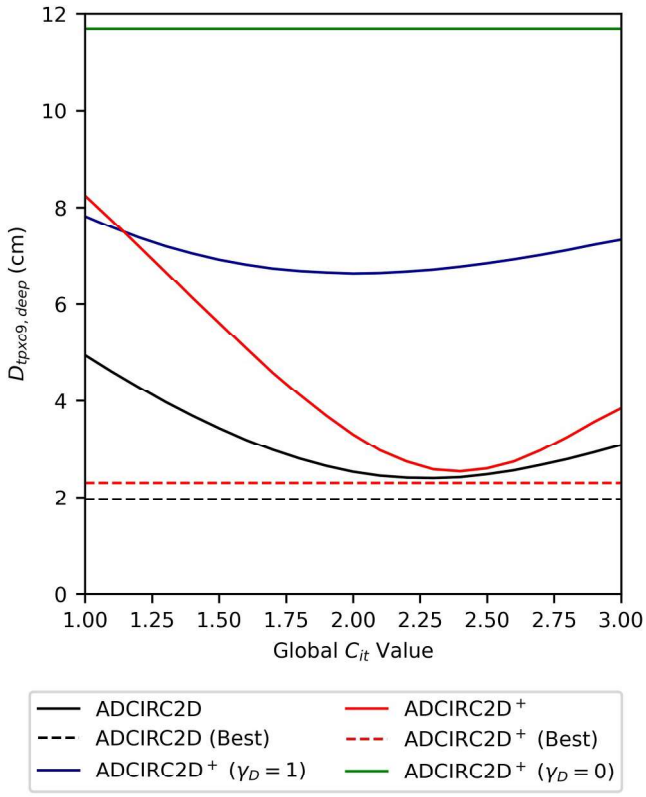

Figure 1. Mean discrepancy compared to TPXO9 in waters deeper than 1,000 m as a function of varying spatially constant global C_{it} values. Solid black and red curves represent ADCIRC2D and ADCIRC2D$^+$ respectively. The solid green curve shows ADCIRC2D$^+$ when $\gamma_D = 0$ for all space and time. The solid blue curve shows ADCIRC2D$^+$ when $\gamma_D = 1$ for all space and time. Dashed reference lines show $D_{tpxo9,deep}$ of the best ADCIRC2D (black) and ADCIRC2D$^+$ (red) solutions. These solutions are a result of spatially varying C_{it} values through the error minimization technique described in Blakely et al. (2022) and Section 3.2. ADCIRC2D curve is reproduced from Blakely et al. (2022).

where, A^k and θ^k denote the amplitude and phase of tidal constituent k. Subscripts m and o denote modeled and observed (either from tide gauge data or from TPXO9), and A_i and D_i represent the area and mean discrepancy for each element in the finite element mesh. Tidal errors at stations are reported as mean discrepancies from observed tidal harmonics. The overall mean discrepancy for these stations $\left(\overline{D}_{station}\right)$ was calculated for deep ($h \geq 1000$ m); shallow and shelf ($20 < h \leq 1000$ m); and coastal ($h \leq 20$ m) stations as:

$$\overline{D}_{station} = \frac{\sum_i D_i}{N} \tag{9}$$

where, D_i is the discrepancy at station i (Equation 7) and N is the number of stations. Both global and station error statistics are calculated for the major semidiurnal (M_2), major diurnal (K_1), as well as for the combined 8 major tidal constituents.

When comparing to observed water levels from GESLA, normalized variance $\left(\gamma^2\right)$ (Kodaira et al., 2016), model skill (Willmott, 1981), and root mean squared error are calculated for η_{TWL}, $\overline{\eta}_{30}$, and η_{NTR} where,

$$\gamma^2 = \frac{\mathrm{Var}(\eta_m - \eta_o)}{\mathrm{Var}(\eta_o)} \tag{10}$$

$$Skill = 1 - \frac{\int_0^T (\eta_m - \eta_o)^2 dt}{\int_0^T \left(|\eta_m - \overline{\eta}_o| + |\eta_o - \overline{\eta}_o|\right)^2 dt} \tag{11}$$

$$RMSE = \left[\frac{1}{T}\int_0^T (\eta_m - \eta_o)^2 dt\right]^{\frac{1}{2}} \tag{12}$$

Var denotes the variance in time, the subscripts m and o denote modeled and observed respectively, and T is the time period of interest. For normalized variance $\gamma^2 = 0$ denotes perfect agreement of the modeled and observed signal and $\gamma^2 \geq 1$ is no better than a constant prediction. *Skill* (or "index of agreement") varies from 0 to 1 with 1 being a perfect match between observed and modeled values and 0 being perfect disagreement. In this case, *RMSE* is the time averaged root mean square error. In calculating all three error statistics, observations and model results are independently demeaned over the whole three-year hindcast period in order to account for differences between the datums used in reporting total water level observations and the model datum.

4. Results and Discussion

4.1. Tidal Results of ADCIRC2D$^+$

In this section, we first discuss the necessity and impacts of the modification of the internal wave drag tensor by γ_D. This is followed by a presentation of the tidal results of the full three-year hindcasts.

4.1.1. Impact of γ_D on Tidal Solutions

To highlight the impact of including γ_D in the baroclinically-coupled ADCIRC2D$^+$ model, tidal simulations were performed wherein spatially constant global C_{it} values were varied between 1.00 and 3.00 for ADCIRC2D; ADCIRC2D$^+$; ADCIRC2D$^+$ where no filtering was applied to the internal tide dissipation term $\left(\gamma_D = 1\right)$; and ADCIRC2D$^+$ where internal tide dissipation is not included $\left(\gamma_D = 0\right)$. Figure 1 shows the mean discrepancy compared to TPXO9 in waters deeper than 1,000 m as a function of global C_{it} values for these simulations. As can be seen in the solid blue curve, when the internal wave drag is applied to the total velocity $\left(\gamma_D = 1\right)$ within

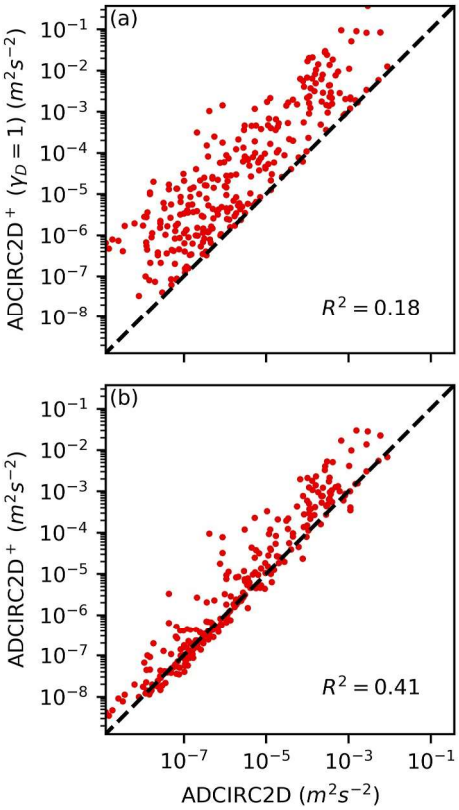

Figure 2. (Time-averaged internal wave drag dissipation at deep-water tide stations: (a) unmodified $(\gamma_D = 1)$ ADCIRC2D$^+$ versus ADCIRC2D, (b) dissipation scaled ADCIRC2D$^+$ versus ADCIRC2D at deep water tide stations.

ADCIRC2D$^+$, the excess dissipation caused by the higher velocities results in significantly degraded tidal solutions due to overdamping regardless of global C_{it} value. While an improvement over the solid green curve where no internal tide dissipation is included $(\gamma_D = 0)$, it is still worse than the results of the solid black, uncoupled, ADCIRC2D curve by a fairly constant three to four cm. However, when the internal tide dissipation tensor is modified by γ_D, as seen in the solid red line, the response of $D_{tpxo9,deep}$ to changing C_{it} is much more similar to barotropic ADCIRC2D, indicating that this parameter is successfully bringing the internal tide dissipation within the baroclinically-coupled model closer to that seen in the barotropic model. After estimating optimal values for C_{it} and Manning's n as described in Section 3.1, the "best" solutions using our optimal, spatially varying Manning's n and C_{it} values show improvement over the best spatially constant C_{it} value on the order of ~0.5 cm for both ADCIRC2D (black dashed line) and ADCIRC2D$^+$ (red dashed line). This indicates that even with optimized friction coefficients, the unmodified, coupled model $(\gamma_D = 1)$ would still underperform our barotropic model.

Figure 2 shows the three-year time-averaged dissipation due to internal wave drag at the 209 deep-water tide gauges (>150 m depth). As Figure 2a clearly shows, the unmodified internal wave drag $(\gamma_D = 1)$ of ADCIRC2D$^+$ consistently over-dissipates compared to ADCIRC2D. This extra dissipation alters the dynamics of the global ocean and greatly changes global tides. (See Blakely et al. (2022) for an examination of the sensitivity of the internal wave drag parameterization.). As is shown in Figure 2b, by using the γ_D adjustment the time-averaged dissipation due to internal wave drag in the baroclinically coupled model at the deep-water stations is in significantly better agreement with the barotropic model. As can be seen in the curve of mean discrepancy versus global C_{it} value for the dissipation scaled case in Figure 1, and we will show in Section 4.1.2, this better agreement results in significantly more accurate tides within our coupled system.

Table 1
Global Tidal Error Statistics Compared to TPXO9 and Tide Gauges

Constituent	Metric	ADCIRC2D	ADCIRC2D$^+$
M_2	$\overline{D}_{tpxo,deep}$ (cm)	1.95	2.27
	$\overline{D}_{tpxo,shallow}$ (cm)	11.02	12.16
	$\overline{D}_{tpxo,total}$ (cm)	4.11	4.54
	$\overline{D}_{station,deep}$ (cm)	2.24	2.73
	$\overline{D}_{station,shallow+shelf}$ (cm)	6.86	7.82
	$\overline{D}_{station,coastal}$ (cm)	11.10	11.26
K_1	$\overline{D}_{tpxo,deep}$ (cm)	0.75	1.06
	$\overline{D}_{tpxo,shallow}$ (cm)	5.17	4.91
	$\overline{D}_{tpxo,total}$ (cm)	1.97	2.10
	$\overline{D}_{station,deep}$ (cm)	0.88	1.42
	$\overline{D}_{station,shallow+shelf}$ (cm)	2.27	2.77
	$\overline{D}_{station,coastal}$ (cm)	3.02	3.13
major 8	$\overline{D}_{tpxo,deep}$ (cm)	2.51	3.19
	$\overline{D}_{tpxo,shallow}$ (cm)	10.35	11.65
	$\overline{D}_{tpxo,total}$ (cm)	4.10	4.82
	$\overline{D}_{station,deep}$ (cm)	2.85	3.83
	$\overline{D}_{station,shallow+shelf}$ (cm)	6.67	7.80
	$\overline{D}_{station,coastal}$ (cm)	12.07	12.44

4.1.2. Tidal Results of Three-Year Hindcasts

As can be seen in Table 1, tidal errors between ADCIRC2D and ADCIRC2D$^+$ are comparable, but are degraded in ADCIRC2D$^+$ by ~10%–20% depending on the statistic. As can be seen in Figures 3a and 3b, mean discrepancy of the M_2 tide in the Atlantic and Indian Oceans shifted but generally remained the same on average, the Pacific and Southern Seas, on the other hand, saw general degradation. Errors in the K_1 constituent (Figures 3c and 3d), as well as the combined mean discrepancy of the 8 major constituents (Figures 3e and 3f), saw degradation throughout most of the oceans.

We attribute the error increases to the remaining discrepancy in the velocity used in the internal tide drag. While the 25-hr lagged average filter used in γ_D described in Section 2.3 removes a large amount of sub-tidal energy, it is not able to remove it completely, leaving some pollution in the velocity signal. Additionally, the 25-hr lagged filter introduces some phase lag, which alters the timing of internal tide dissipation, altering the resulting modeled tides. Finally, the differences between the observation-based WOD climatology and GOFS3.1 climatology could be contributing to the degradation of the tidal solutions.

Figure 4 shows the tidal results compared to global tide stations separated into coastal ($[0, 20)$ meters depth at the station), shallow and shelf ($[20, 1000)$), and deep ocean ($[1000, h_{sta,max}]$) depths. This binning helps to separate out those stations which have poor results due to being resolution limited. As can be seen in the violin plots, the "coastal" tide gauges have both higher median errors as well as a larger deviation than the "shallow" stations. With higher resolution, these coastal stations could be improved.

Altogether, as will be shown in Section 4.2, the slight degradation in tidal results is more than offset by improvements in density-driven sea levels.

4.2. Water Level Results of ADCIRC2D$^+$

Table 2 shows the summary statistics for η_{TWL}, $\overline{\eta}_{30}$, and η_{NTR} of both ADCIRC2D and ADCIRC2D$^+$ compared to GESLA stations. In order to help account for stations which are in complex coastal zones, both mean and median error statistics of the GESLA stations are reported.

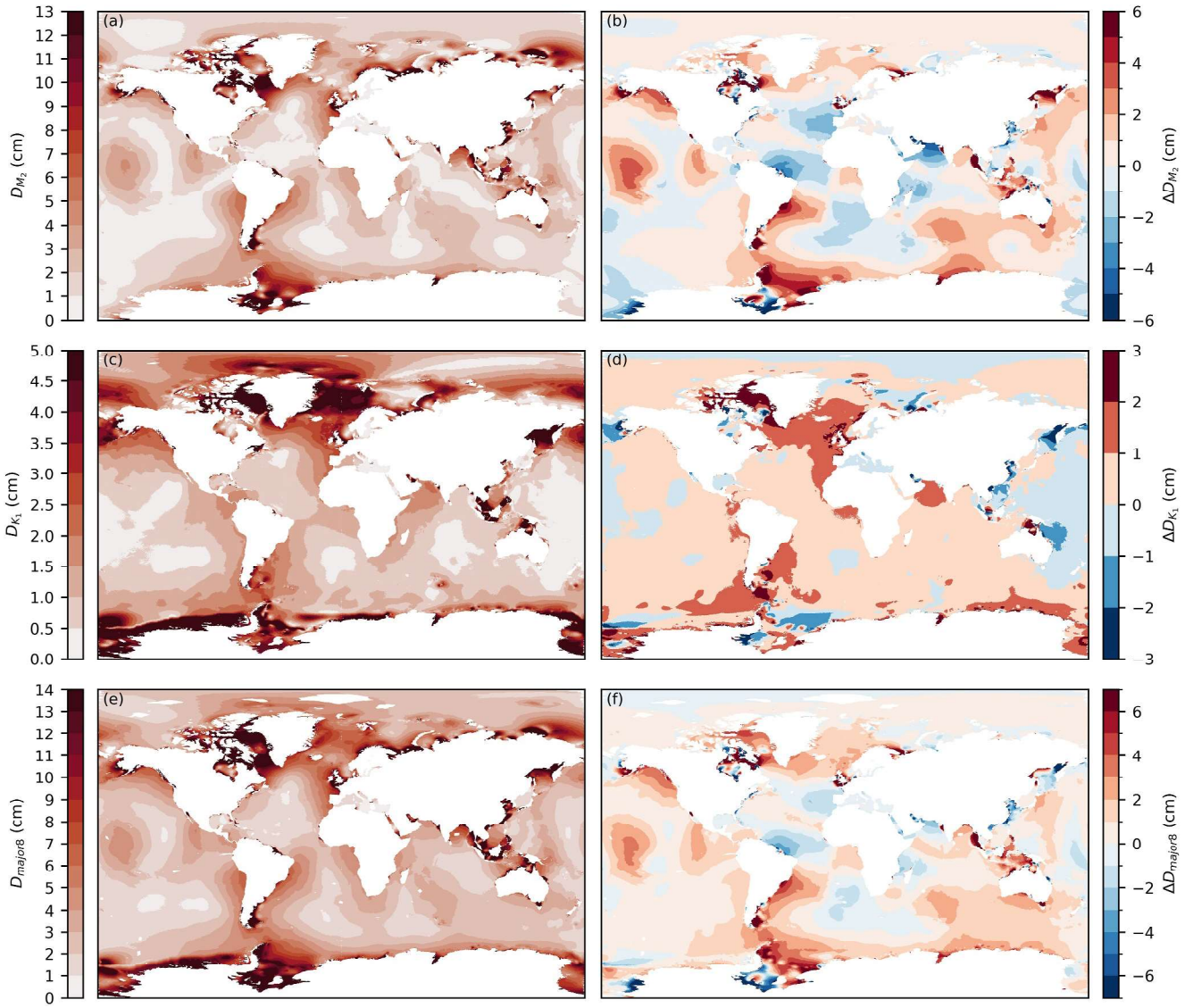

Figure 3. Panels (a), (c), and (e) show the mean discrepancy compared to TPXO9 for ADCIRC2D$^+$ for M_2, K_1, and 8 major constituents respectively. Panels (b), (d), and (f) show the difference in mean discrepancy as compared to ADCIRC2D calculated as D_{ADCIRC2D^+}-D_{ADCIRC2D}.

Unlike the tidal results, the coupled ADCIRC2D$^+$ model outperforms the barotropic ADCIRC2D model for all error metrics. With an improvement of 0.83 cm (1.86 cm) in mean (median) RMSE and similar improvements seen in model skill and normalized variance for total water levels, it is clear that the inclusion of density-driven terms—even in the heterogeneously coupled form in ADCIRC2D$^+$—greatly improves model results.

These improvements become even more clear when comparing the 30-day mean sea levels. The improvement in mean (median) model skill from 0.65 (0.70) in ADCIRC2D to 0.88 (0.94) in ADCIRC2D$^+$, shows that the inclusion of GOFS3.1 forcing within ADCIRC is paramount to capturing low frequency sea level variations. Nontidal residuals also see modest improvements due to the inclusion of density-driven terms. With mean (median) skill improving from 0.75 (0.81) to 0.81 (0.86) from ADCIRC2D to ADCIRC2D$^+$.

Table 3 reports the error statistics of both 30-day mean sea levels and non-tidal residuals of ADCIRC2D$^+$ and GOFS3.1. While not as drastic of an improvement as is seen when comparing mean sea levels of ADCIRC2D and ADCIRC2D$^+$, there are improvements in all error statistics on the order of 5%–30% when comparing ADCIRC2D$^+$ and GOFS3.1. These improvements are likely due to increased resolution in ADCIRC allowing for more accurate representation of bathymetry, especially in regions which are particularly sensitive to frictional

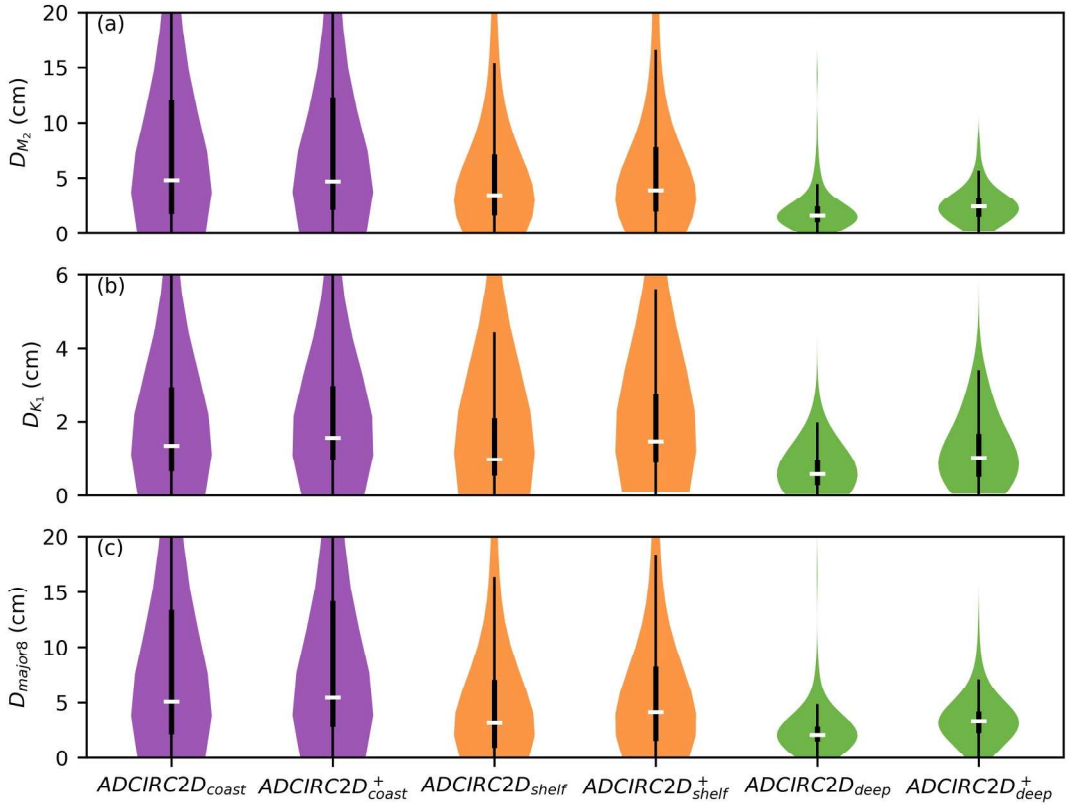

Figure 4. Mean discrepancy compared to global tide gauges separated into coastal ($0 \leq h_{sta} < 20$ m) (purple), shallow and shelf ($20 \leq h_{sta} < 1000$ m) (orange), and deep ($h_{sta} \geq 1000$ m) (green) stations for (a) M_2 (b) K_1 and (c) major 8 constituents. White horizontal lines mark the median errors, thick black lines span the interquartile range (IQR), and thin black lines extend to ±1.5IQR of Q2 and Q3. Note the different limits on the K_1 errors.

perturbation such as Hudson Bay (Blakely et al., 2022). Consistent with W. J. Pringle et al. (2019), the skill of the ADCIRC model when comparing non-tidal sea levels is much higher than that seen in GOFS3.1, with statistics improving from 30% to 50%. The main cause of this improvement is undoubtedly the higher resolution model. With more accurate representation of continental shelves, it is possible to capture resonance across shelves, which can amplify wind-driven water levels.

Figures 5 and 6 provide a visual representation of the improvements in error statistics due to the inclusion of baroclinic forcing via GOFS3.1 in ADCIRC2D^{+}. As can be seen in Figure 5, not only does the inclusion of BPG within ADCIRC improve the mean and median error statistics, it greatly reduces the range of errors seen within the model. This is particularly noticeable in model skill of 30-day mean sea levels (Figure 5a). While not quite as dramatic as the improvements in long-term sea levels, both total water levels and nontidal residuals are also improved in ADCIRC2D^{+} as compared to ADCIRC2D. Of particular note is that the nontidal residual error statistics do not appear to decrease in variability as much as total water levels and long-term sea levels, helping to explain the relatively small improvements in global mean and median error statistics seen in Table 2.

Figure 6 shows the change in error statistics at GESLA stations around the globe. This allows for a sense of the spatial improvements due to inclusion of density-driven terms that are present in ADCIRC2D^{+}. Echoing the improvements in long-term sea levels seen in Figures 5, 6b, 6e, and 6h show that—with some few exceptions—the representation of long-term sea levels is dramatically improved globally in ADCIRC2D +. Particularly when looking at RMSE (Figure 6d) of total water levels, it is clear that areas of particularly high baroclinic activity (such as the US East Coast and the Eastern coast of Asia) see improvement in total water levels with the inclusion of baroclinic forcing. While some areas seem to degrade in RMSE, model skill (Figure 6a) and normalized variance (Figure 6g) do not see large degradation in performance. Finally, Figures 6c, 6f, and 6i help to explain the relatively small changes in error statistics seen in nontidal residuals. While Figure 6c shows good improvement

Table 2
Mean and Median Error Statistics Compared to GESLA Stations of ADCIRC2D and ADCIRC2D$^+$ Models

Water level type	Metric	ADCIRC2D	ADCIRC2D$^+$
Total Water Level	Mean Skill (–)	0.94	0.96
	Mean RMSE (cm)	16.09	15.26
	Mean γ^2 (–)	0.22	0.17
	Median Skill (–)	0.97	0.98
	Median RMSE (cm)	10.05	8.19
	Median γ^2 (–)	0.11	0.09
30-day Mean Sea Level	Mean skill (–)	0.65	0.88
	Mean RMSE (cm)	8.13	5.81
	Mean γ^2 (–)	0.64	0.29
	Median skill (–)	0.70	0.94
	Median RMSE (cm)	6.00	3.45
	Median γ^2 (–)	0.61	0.17
Nontidal Residual	Mean Skill (–)	0.75	0.81
	Mean RMSE (cm)	10.07	10.05
	Mean γ^2 (–)	0.61	0.63
	Median Skill (–)	0.81	0.86
	Median RMSE (cm)	6.84	6.48
	Median γ^2 (–)	0.58	0.49

when measured using model skill at mid-latitudes, RMSE (Figure 6f) and normalized variance (Figure 6i) show that while the Grand Banks off the Northern Canadian coast, the Japan Sea, and the Pacific near Hawaii improve, the Pacific off the Americas, the Indian Ocean, and Northern Australia degrade, helping to explain the lack of wholesale improvement in global statistics seen in total water levels and 30-day mean sea levels.

Figure 7 shows a selection of time series at stations with observations, ADCIRC2D, and ADCIRC2D$^+$ results. As suggested by the error statistics in Table 2, the, total water level time series show modest improvement; however, the performance of ADCIRC2D$^+$ in capturing long-term sea levels far outstrips that of ADCIRC2D. This is most

Table 3
Mean and Median Error Statistics Compared to GESLA Stations of ADCIRC2D$^+$ and GOFS3.1 Models

Water level type	Metric	ADCIRC2D$^+$	GOFS3.1
30-day Mean Sea Level	Mean skill (–)	0.88	0.82
	Mean RMSE (cm)	5.18	6.14
	Mean γ^2 (–)	0.30	0.45
	Median skill (–)	0.94	0.88
	Median RMSE (cm)	3.40	4.47
	Median γ^2 (–)	0.19	0.55
Nontidal Residual	Mean Skill (–)	0.80	0.50
	Mean RMSE (cm)	9.54	14.18
	Mean γ^2 (–)	0.61	1.29
	Median Skill (–)	0.86	0.56
	Median RMSE (cm)	6.11	10.62
	Median γ^2 (–)	0.49	1.18

Note. Note that both sets of error statistics were calculated with the reduced set of GESLA records.

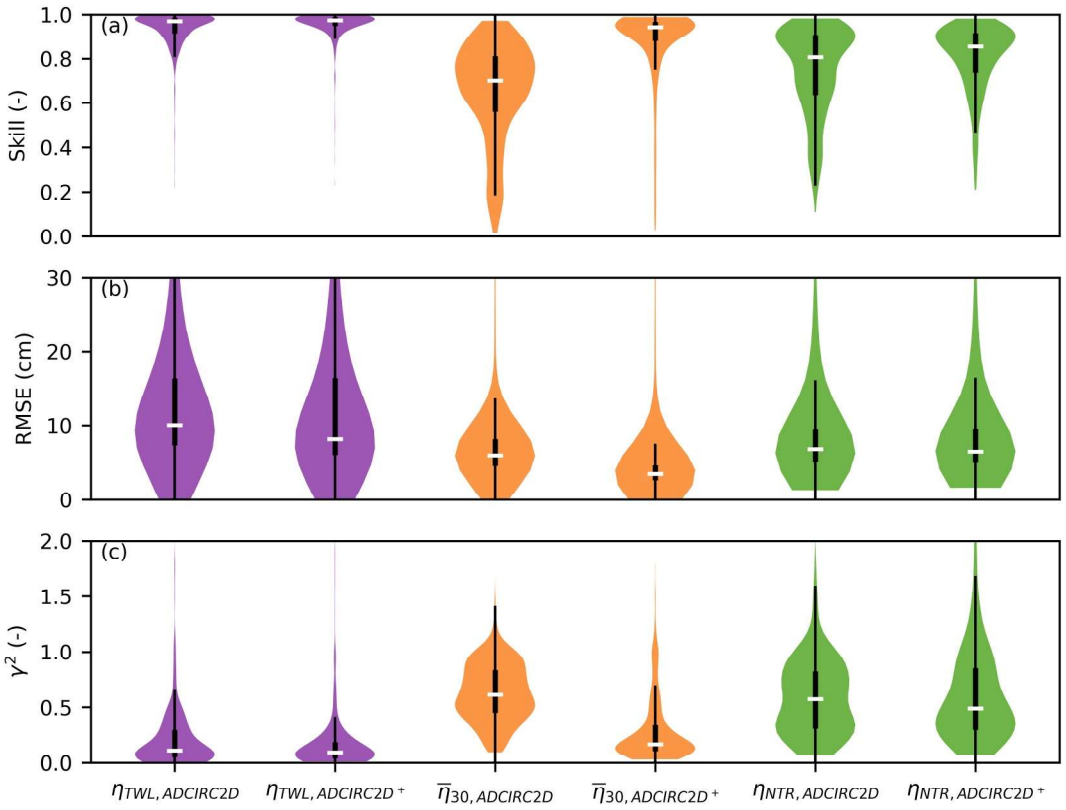

Figure 5. Error statistics compared to GESLA stations of total water levels (purple), 30-day mean sea levels (orange) and nontidal residuals (green) of ADCIRC2D and ADCIRC2D$^+$. Model skill (a), RMSE (b), and normalized variance (c) are reported. White horizontal lines mark median errors, thick black lines span the interquartile range (IQR), and thin black lines span from ±1.5IQR of Q2 and Q3.

noticeable in Figures 7b, 7e, and 7h, which highlight the improvements in 30-day mean sea levels seen in ADCIRC2D$^+$, with San Juan, Hanimadhoo, and Toyama seeing drastic improvement in the representation of long-term sea levels. While less drastic, due in part to lower baroclinic activity, Montauk, Los Angeles, and Tredge all show improvement in long-term sea levels. Nome, Alaska, which is on the well-mixed Bering Shelf, does not see much change in water levels with the inclusion of baroclinic forcing, which is expected in highly barotropic regions. Additionally, as was explored in W. J. Pringle et al. (2019), the inclusion of baroclinic forcing within the depth-averaged ADCIRC2D helps to capture the post-hurricane drawdown at San Juan (Figures 7a–7c) after Hurricane Maria, which made landfall in Puerto Rico on 20 September 2017. This is particularly visible in the plot of the nontidal residuals (Figure 7c).

Finally, Figure 8 shows the power spectral density (PSD) at the stations plotted in Figure 7. At the lower subtidal frequencies (particularly those above fortnightly periods, <0.073 cycles per day), ADCIRC2D$^+$ has increased energy in agreement with observations. There is still some remaining intra-tidal energy that is missing from the models especially at the mid-ocean island stations, which suggests wave action could be the cause. As mentioned above, there is relatively little difference between ADCIRC2D and ADCIRC2D$^+$ seen in the highly-barotropic Bering Shelf at Nome (Figure 8d).

5. Summary and Conclusions

In this article, we have detailed some of the modifications required in order to maintain high tidal accuracy in a depth-averaged, high coastal resolution total water level numerical model heterogeneously coupled to an OGCM with coarser coastal resolution. Of particular importance is ensuring that internal tide dissipation is correctly represented in the depth-averaged model. If left unmodified, the increase in kinetic energy in the deep ocean due to higher deep-ocean velocities—and corresponding increase in dissipation due to the internal wave drag

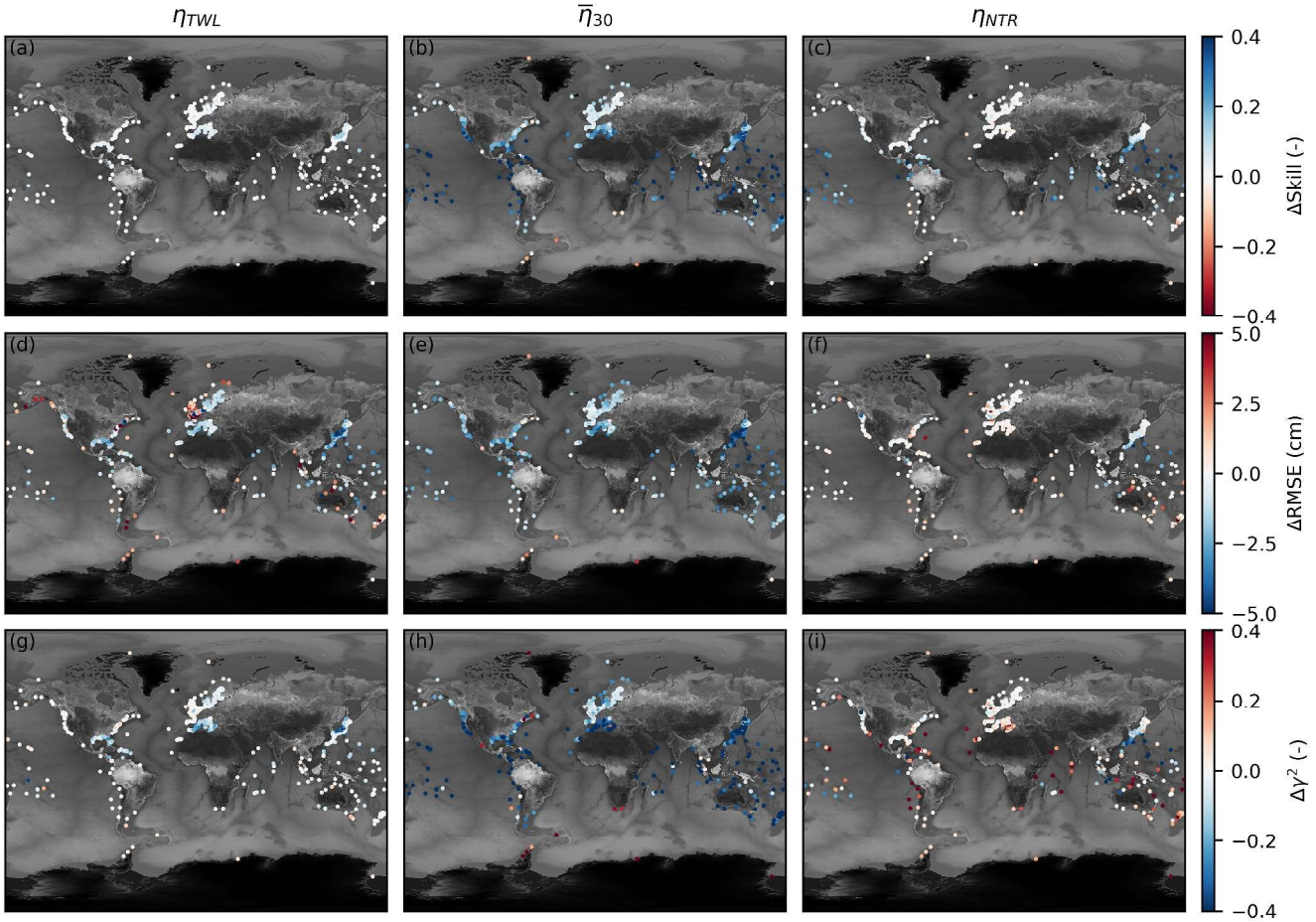

Figure 6. Panels (a), (d), and (g) show the change in Skill, RMSE, and normalized variance respectively of total water levels from ADCIRC2D to ADCIRC2D$^+$. Panels (b), (e), and (h) show the same for 30-day mean sea levels. Panels (c), (f), and (i) show the same for nontidal residuals. Colormaps are set so that blue indicates improvement while red indicates degradation. Basemap courtesy of NASA (n.d.).

parameterization in the SWEs—greatly degrades the fidelity and accuracy of tidal results within the coupled system with respect to the uncoupled model. In order to address this degradation, the internal wave drag tensor is scaled by the ratio of an estimated "tidal" dissipation and the "total" dissipation in order to force the internal tide dissipation within the coupled model to approximate that seen in the fully barotropic model. By scaling the tensor by a single parameter, we preserve the numerical stability of the directional internal tide dissipation parameterization discussed and examined in Lyard et al. (2006); W. J. Pringle, Wirasaet, Suhardjo, et al. (2018); Blakely et al. (2022).

With this modification to the internal wave drag parameterization, as well as some parameter estimation to find appropriate C_{it} values for the baroclinic model, we are able to bring the mean discrepancy compared to TPXO9 in the deep ocean of the baroclinic model from a minimum of ∼6 centimeters in the unfiltered model down to 2.27 cm in ADCIRC2D$^+$, which is quite close to the 1.95 cm obtained in the barotropic ADCIRC2D simulations.

Despite the slight degradation in tidal results, total water level results in ADCIRC2D$^+$ are greatly improved over those seen in ADCIRC2D. The median RMSE of total water levels, 30-day mean sea levels, and nontidal residuals improve from 10.05 to 8.19 cm; from 6.00 to 3.45 cm; and from 6.84 to 6.48 cm compared to GESLA water level stations respectively. Of particular import is the improvement in the representation of low frequency sea level variations, with median normalized error variance of the 30-day moving mean reduced from 0.61 in ADCIRC2D, which is only slightly better than a constant prediction, to 0.17 in ADCIRC2D$^+$.

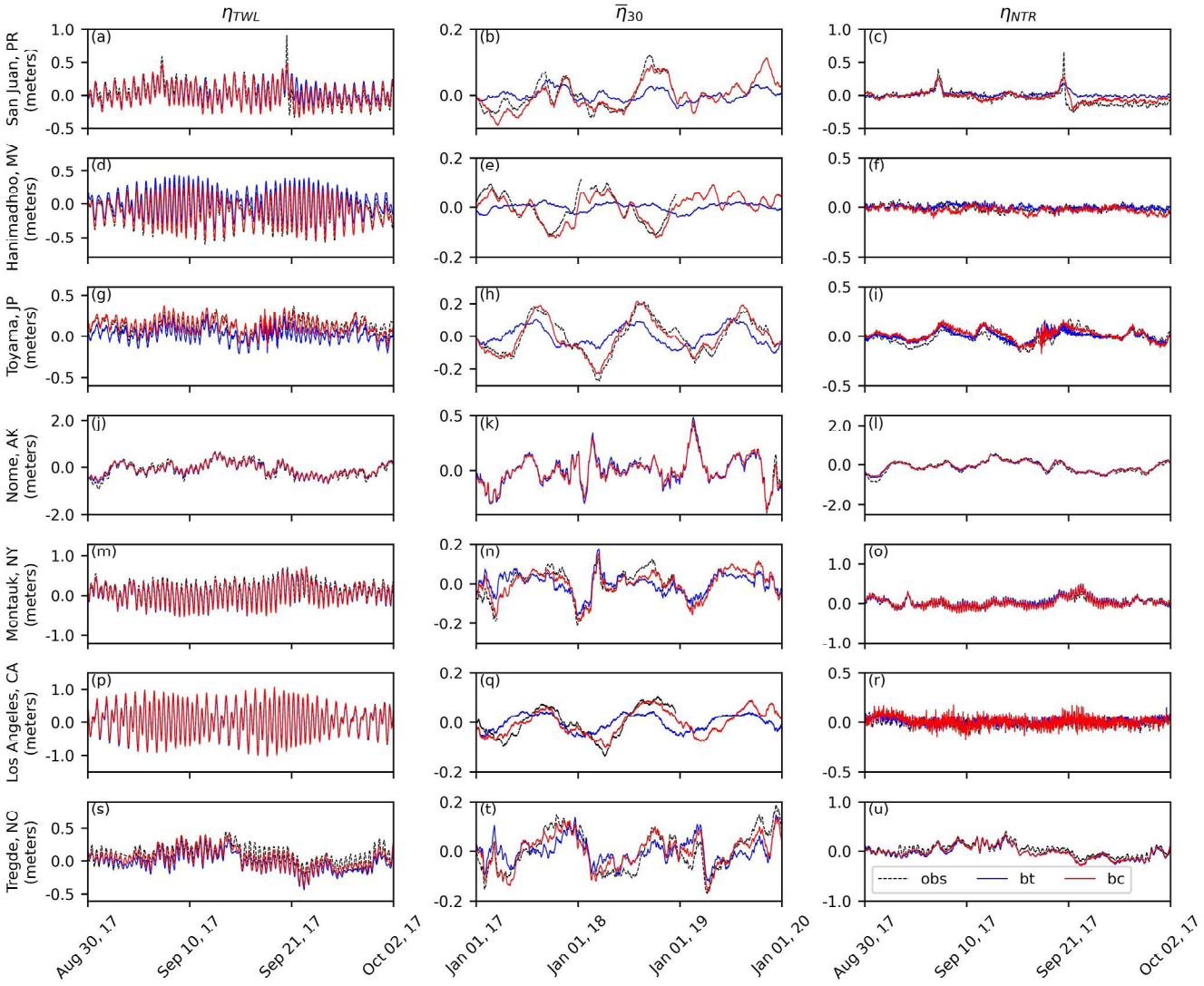

Figure 7. Time series at a selection of stations of total water levels (a, d, g, j, m, p, s); 30-day mean sea levels (b, e, h, k, n, q, t); and nontidal residuals (c, f, i, l, o, f, u). Time series are independently demeaned. Observations are plotted as black dashed lines, ADCIRC2D results as blue solid lines, and ADCIRC2D$^+$ as red solid lines.

In addition, this improvement to modeling the low frequency sea level variations comes at an extremely modest computational cost. Compared to purely barotropic ADCIRC, ADCIRC2D$^+$ only increases runtime by approximately 11% due to the need to download and pre-process the GOFS3.1 forecast data, which allows for this methodology to be deployed in a forecasting framework such as NOAA's STOFS-2D-Global, which is currently an ongoing upgrade to that forecasting system.

Future directions of inquiry that follow from this work include developing a better filter to estimate the tidal velocity and incorporating lee wave dissipation seen at non-tidal frequencies in the coupled model. By using a filter which removes more non-tidal energy from the velocity spectrum, or by reducing the phase lag of the filter, we would expect even more accuracy in our tidal results. Additionally, testing OGCMs other than GOFS3.1 could provide valuable information about both the OGCMs as well as the sensitivities of the coupled system to different salinity and temperature fields. Finally, implementing the heterogeneous coupling of ADCIRC2D$^+$ with a higher resolution computational domain will be of vital importance in accurately capturing water levels in complex coastal zones.

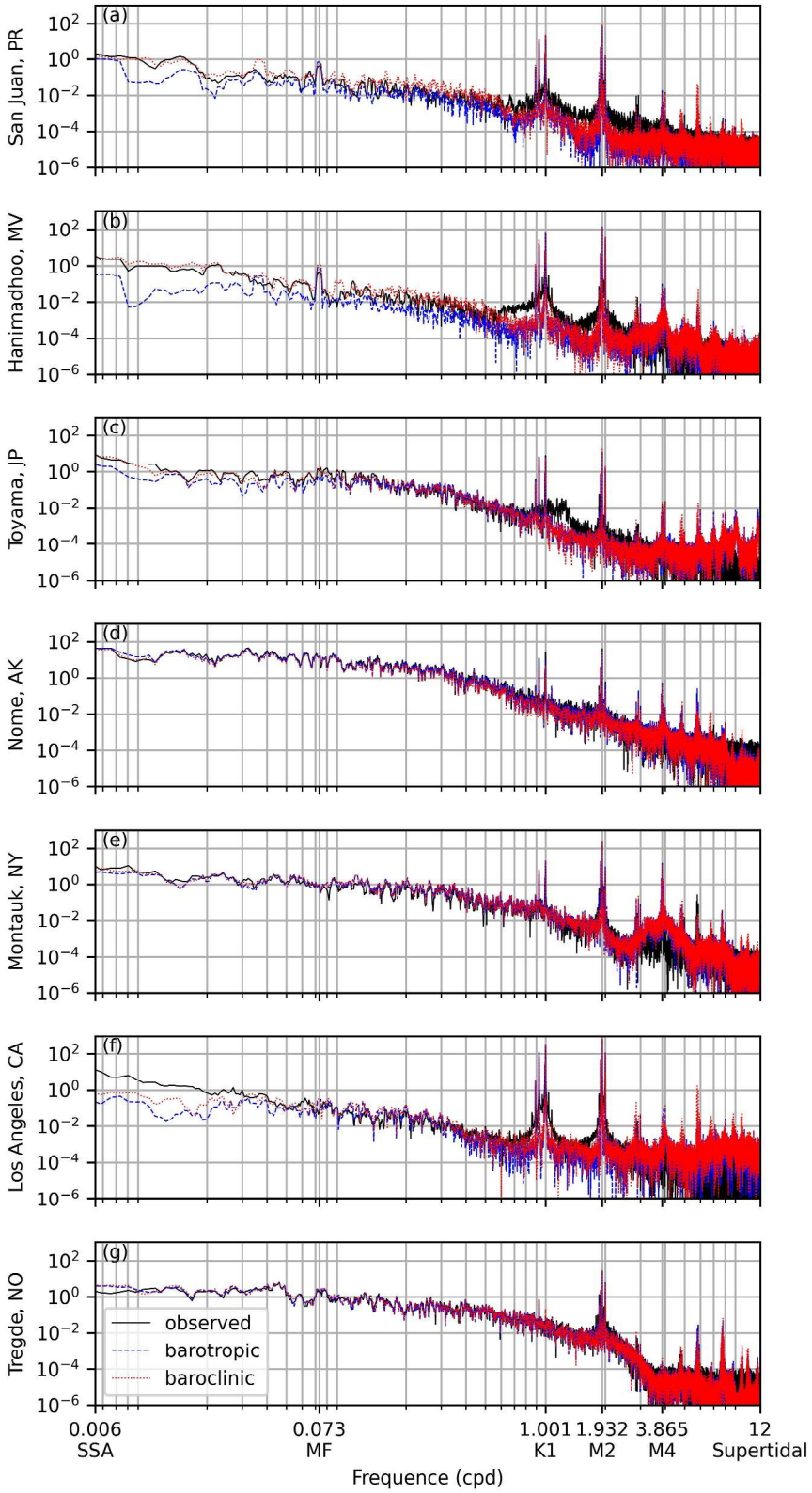

Figure 8. Power spectral density at stations plotted in Figure 7. Note that the cutoff of 12 cycles per day is due to the sampling frequency of the GESLA observations being one hour, causing the folding frequency to be 12 cycles per day.

Data Availability Statement

The source code for ADCIRC is publicly available under the GNU Lesser General Public License 3.0 at https://github.com/adcirc/adcirc. Meteorological forcing from CFSv2 can be found through the official NCEP web portal at http://cfs.ncep.noaa.gov/. GOFS3.1 data is available online at https://www.hycom.org/. The full tide gauge data set used can be found at coast.nd.edu. GESLAv3 is publicly available at https://doi.org/10.5285/d21a496a-a48e-1f21-e053-6c86abc08512 (Haigh, 2022a) and https://doi.org/10.5285/d21a496a-a48f-1f21-e053-6c86abc08512 (Haigh, 2022b). The computational mesh and selected results, including water level time series at selected stations can be found at Blakely (2024). The OceanMesh2D V3.3 software used to create the mesh in the study is available from https://zenodo.org/badge/DOI/10.5281/zenodo.4386220.svg and is developed at https://github.com/CHLNDDEV/OceanMesh2D under the GNU General Public License 3.0 (W. Pringle & Roberts, 2020).

Acknowledgments

We thank the editors and three anonymous reviewers for their thoughtful and constructive feedback on this manuscript. This study was funded through the National Science Foundation PREEVENTS Track 2 grant ICER-1855047. Joannes J. Westerink was supported in part by the Joseph and Nona Ahearn endowment at the University of Notre Dame. Joannes J. Westerink and Damrongsak Wirasaet were supported in part by Department of Energy Grant DOE DE-SC0021105. William J. Pringle was supported by the U.S. National Oceanic and Atmospheric Administration (NOAA) through a Virginia Institute of Marine Science subaward under Strategic Partnership Project agreement A23089 to Argonne National Laboratory through U.S. Department of Energy contract no. DE-AC02-06CH11357. Steven Brus was supported by the Earth System Model Development program area of the U.S. Department of Energy, Office of Science, Office of Biological and Environmental Research as part of the Office of Science Early Career Research Program.

References

Arbic, B. K. (2022). Incorporating tides and internal gravity waves within global ocean general circulation models: A review. *Progress in Oceanography*, *206*, 102824. https://doi.org/10.1016/j.pocean.2022.102824

Arbic, B. K., Alford, M. H., Ansong, J. K., Buijsman, M. C., Ciotti, R. B., Farrar, J. T., et al. (2018). A primer on global internal tide and internal gravity wave continuum modeling in HYCOM and MITgcm. *New Frontiers in Operational Oceanography*. https://doi.org/10.17125/GOV2018.CH13

Arbic, B. K., & Garrett, C. (2010). A coupled oscillator model of shelf and ocean tides. *Continental Shelf Research*, *30*(6), 564–574. https://doi.org/10.1016/j.csr.2009.07.008

Arbic, B. K., Wallcraft, A. J., & Metzger, E. J. (2010). Concurrent simulation of the eddying general circulation and tides in a global ocean model. *Ocean Modelling*, *32*(3–4), 175–187. https://doi.org/10.1016/j.ocemod.2010.01.007

Asher, T. G., Luettich, R. A., Fleming, J. G., & Blanton, B. O. (2019). Low frequency water level correction in storm surge models using data assimilation. *Ocean Modelling*, *144*(September), 101483. https://doi.org/10.1016/j.ocemod.2019.101483

Blakely, C. P. (2024). Data supporting dissipation scaled internal wave drag in a global heterogeneously coupled internal/external mode total water level model [Dataset]. *Zenodo*. https://doi.org/10.5281/zenodo.11550178

Blakely, C. P., Ling, G., Pringle, W. J., Contreras, M. T., Wirasaet, D., Westerink, J. J., et al. (2022). Dissipation and bathymetric sensitivities in an unstructured mesh global tidal model. *Journal of Geophysical Research: Oceans*, *127*(5), e2021JC018178. https://doi.org/10.1029/2021JC018178

Boyer, T. P., Antonov, J. I., Baranova, O. K., Garcia, H. E., Johnson, D. R., Mishonov, A. V., et al. (2013). World ocean database 2013 (Tech. Rep.). https://doi.org/10.7289/V5NZ85MT

Bunya, S., Dietrich, J. C., Westerink, J. J., Ebersole, B. A., Smith, J. M., Atkinson, J. H., et al. (2010). A high-resolution coupled riverine flow, tide, wind, wind wave, and storm surge model for Southern Louisiana and Mississippi. Part I: Model development and validation. *Monthly Weather Review*, *138*(2), 345–377. https://doi.org/10.1175/2009MWR2906.1

Carrère, L., & Lyard, F. (2003). Modeling the barotropic response of the global ocean to atmospheric wind and pressure forcing - Comparisons with observations. *Geophysical Research Letters*, *30*(6), 1275. https://doi.org/10.1029/2002GL016473

Codiga, D. L. (2011). Unified tidal analysis and prediction using the UTide Matlab Functions (Tech. Rep. No. September). https://doi.org/10.13140/RG.2.1.3761.2008

Egbert, G. D., & Erofeeva, S. Y. (2002). Efficient inverse modeling of Barotropic Ocean tides. *Journal of Atmospheric and Oceanic Technology*, *19*(2), 183–204. https://doi.org/10.1175/1520-0426(2002)019⟨0183:EIMOBO⟩2.0.CO;2

Egbert, G. D., & Ray, R. D. (2000). Significant dissipation of tidal energy in the deep ocean inferred from satellite altimeter data. *Nature*, *405*(6788), 775–778. https://doi.org/10.1038/35015531

Garratt, J. R. (1977). Review of drag coefficients over oceans and continents. *Monthly Weather Review*, *105*(7), 915–929. https://doi.org/10.1175/1520-0493(1977)105⟨0915:RODCOO⟩2.0.CO;2

Garrett, C., & Munk, W. (1979). Internal waves in the ocean. *Annual Review of Fluid Mechanics*, *11*(1), 339–369. https://doi.org/10.1146/annurev.fl.11.010179.002011

Green, J. A., & Nycander, J. (2013). A comparison of tidal conversion parameterizations for tidal models. *Journal of Physical Oceanography*, *43*(1), 104–119. https://doi.org/10.1175/JPO-D-12-023.1

Haigh, I. D. (2022a). GESLA version 3: Part 1 [Dataset]. *GESLA*. https://doi.org/10.5285/d21a496a-a48e-1f21-e053-6c86abc08512

Haigh, I. D. (2022b). GESLA version 3: Part 2 [Dataset]. *GESLA*. https://doi.org/10.5285/d21a496a-a48f-1f21-e053-6c86abc08512

Haigh, I. D., Marcos, M., Talke, S. A., Woodworth, P. L., Hunter, J. R., Hague, B. S., et al. (2022). GESLA version 3: A major update to the global higher-frequency sea-level dataset. *Geoscience Data Journal*, *10*(3), 293–314. https://doi.org/10.1002/gdj3.174

Hope, M., Westerink, J., Kennedy, A., Kerr, P., Dietrich, J., Dawson, C., et al. (2013). Hindcast and validation of Hurricane Ike (2008) waves, forerunner, and storm surge. *Journal of Geophysical Research*, *118*(9), 4424–4460. https://doi.org/10.1002/jgrc.20314

Hsiang, S., Kopp, R., Jina, A., Rising, J., Delgado, M., Mohan, S., et al. (2017). Estimating economic damage from climate change in the United States. *Science*, *356*(6345), 1362–1369. https://doi.org/10.1126/science.aal4369

Joyce, B. R., Pringle, W. J., Wirasaet, D., Westerink, J. J., Van der Westhuysen, A. J., Grumbine, R., & Feyen, J. (2019). High resolution modeling of western Alaskan tides and storm surge under varying sea ice conditions. *Ocean Modelling*, *141*, 101421. https://doi.org/10.1016/j.ocemod.2019.101421

Knutson, T., Camargo, S. J., Chan, J. C. L., Emanuel, K., Ho, C.-H., Kossin, J., et al. (2020). Tropical cyclones and climate change assessment: Part II: Projected response to anthropogenic warming. *Bulletin of the American Meteorological Society*, *101*(3), E303–E322. https://doi.org/10.1175/BAMS-D-18-0194.1

Kodaira, T., Thompson, K. R., & Bernier, N. B. (2016). The effect of density stratification on the prediction of global storm surges. *Ocean Dynamics*, *66*(12), 1733–1743. https://doi.org/10.1007/s10236-016-1003-6

Luettich, R. A., & Westerink, J. J. (1992). *ADCIRC: An advanced three-dimensional circulation model for shelves coasts and estuaries, report 1: Theory and methodology of ADCIRC-2DDI and ADCIRC-3DL, Dredging Research Program (Tech. Rep.)*. DRP-92-6, U.S. Army Engineers Waterways Experiment Station.

Lyard, F., Lefevre, F., Letellier, T., & Francis, O. (2006). Modelling the global ocean tides: Modern insights from FES2004. *Ocean Dynamics*, *56*(5), 394–415. https://doi.org/10.1007/s10236-006-0086-x

Lynch, D. R., & Gray, W. G. (1979). A wave equation model for finite element tidal computations. *Computers & Fluids*, *7*(3), 207–228. https://doi.org/10.1016/0045-7930(79)90037-9

McDougall, T. J., & Barker, P. M. (2011). *Getting started with TEOS-10 and the Gibbs Seawater (GSW) oceanographic toolbox*. SCOR/IAPSO WG127.

Metzger, E. J., Helber, R. W., Hogan, P. J., Posey, P. G., Thoppil, P. G., Townsend Tamara, L., et al. (2017). *Global ocean forecast system 3.1 validation testing (Tech. Rep.). MS 39529-5004*. Naval Research Laboratory, Stennis Space Center.

Moftakhari, H. R., AghaKouchak, A., Sanders, B. F., & Matthew, R. A. (2017). Cumulative hazard: The case of nuisance flooding. *Earth's Future*, *5*(2), 214–223. https://doi.org/10.1002/2016EF000494

Munk, W. (1997). Once again: Once again - Tidal friction. *Progress in Oceanography*, *40*(1–4), 7–35. https://doi.org/10.1016/S0079-6611(97)00021-9

NASA. (n.d.). Visible Earth [image repository]. Retrieved from https://visibleearth.nasa.gov/

Nicholls, R. J., Hoozemans, F. M., & Marchand, M. (1999). Increasing flood risk and wetland losses due to global sea-level rise: Regional and global analyses. *Global Environmental Change*, *9*(SUPPL.), S69–S87. https://doi.org/10.1016/S0959-3780(99)00019-9

Nikurashin, M., & Ferrari, R. (2011). Global energy conversion rate from geostrophic flows into internal lee waves in the deep ocean. *Geophysical Research Letters*, *38*(8), L08610. https://doi.org/10.1029/2011GL046576

Pringle, W., & Roberts, K. (2020). CHLNDDEV/OceanMesh2D: OceanMesh2D V3.3 [Software]. *Zenodo*. https://doi.org/10.5281/zenodo.4386220

Pringle, W. J. (2017). Major tidal constituents for the Indian Ocean and Western Pacific Basin. https://doi.org/10.17632/tjyjn56jbf.1

Pringle, W. J., Gonzalez-lopez, J., Joyce, B., Westerink, J. J., & van der Westhuysen, A. J. (2019). Baroclinic coupling improves depth-integrated modeling of coastal sea level variations around Puerto Rico and the U.S. Virgin Islands. *Journal of Geophysical Research: Oceans*, *124*(3), 2196–2217. https://doi.org/10.1029/2018JC014682

Pringle, W. J., Wirasaet, D., Roberts, K. J., & Westerink, J. J. (2021). Global storm tide modeling with ADCIRC v55: Unstructured mesh design and performance. *Geoscientific Model Development*, *14*(2), 1125–1145. https://doi.org/10.5194/gmd-14-1125-2021

Pringle, W. J., Wirasaet, D., Suhardjo, A., Meixner, J., Westerink, J. J., Kennedy, A. B., & Nong, S. (2018a). Finite-element barotropic model for the Indian and Western Pacific Oceans: Tidal model-data comparisons and sensitivities. *Ocean Modelling*, *129*, 13–38. https://doi.org/10.1016/j.ocemod.2018.07.003

Pringle, W. J., Wirasaet, D., & Westerink, J. J. (2018b). Modifications to internal tide conversion parameterizations and implementation into barotropic ocean models. *EarthArXiv*, *9*. https://doi.org/10.31223/osf.io/84w53

Roberts, K. J., Pringle, W. J., & Westerink, J. J. (2019). OceanMesh2D 1.0: MATLAB-based software for two-dimensional unstructured mesh generation in coastal ocean modeling. *Geoscientific Model Development*, *12*(5), 1847–1868. https://doi.org/10.5194/gmd-12-1847-2019

Saha, S., Moorthi, S., Wu, X., Wang, J., Nadiga, S., Tripp, P., et al. (2014). The NCEP climate forecast system version 2. *Journal of Climate*, *27*(6), 2185–2208. https://doi.org/10.1175/JCLI-D-12-00823.1

Shakespeare, C. J. (2020). Interdependence of internal tide and lee wave generation at abyssal hills: Global calculations. *Journal of Physical Oceanography*, *50*(3), 655–677. https://doi.org/10.1175/JPO-D-19-0179.1

Slobbe, D. C., Verlaan, M., Klees, R., & Gerritsen, H. (2013). Obtaining instantaneous water levels relative to a geoid with a 2D storm surge model. *Continental Shelf Research*, *52*, 172–189. https://doi.org/10.1016/j.csr.2012.10.002

Wang, P., Bernier, N. B., & Thompson, K. R. (2022). Adding baroclinicity to a global operational model for forecasting total water level: Approach and impact. *Ocean Modelling*, *174*, 102031. https://doi.org/10.1016/j.ocemod.2022.102031

Wang, X., Chao, Y., Shum, C. K., Yi, Y., & Fok, H. S. (2012). Comparison of two methods to assess ocean tide models. *Journal of Atmospheric and Oceanic Technology*, *29*(8), 1159–1167. https://doi.org/10.1175/JTECH-D-11-00166.1

Westerink, J. J., Luettich, R. A., Feyen, J. C., Atkinson, J. H., Dawson, C., Roberts, H. J., et al. (2008). A basin- to channel-scale unstructured grid hurricane storm surge model applied to Southern Louisiana. *Monthly Weather Review*, *136*(3), 833–864. https://doi.org/10.1175/2007MWR1946.1

Willmott, C. J. (1981). On the validation of models. *Physical Geography*, *2*(2), 184–194. https://doi.org/10.1080/02723646.1981.10642213

Zhang, Y. J., Fernandez-Montblanc, T., Pringle, W., Yu, H.-C., Cui, L., & Moghimi, S. (2023). Global seamless tidal simulation using a 3D unstructured-grid model (SCHISM v5.10.0). *Geoscientific Model Development*, *16*(9), 2565–2581. https://doi.org/10.5194/gmd-16-2565-2023